Supporting Information for "Gradual inlet expansion and barrier drowning under most sea level rise scenarios"

Laura Portos-Amill[1,2], Jaap H. Nienhuis[3], Huib E. de Swart[1]

[1]Institute for Marine and Atmospheric Research, Department of Physics, Utrecht University, NL

[2]Water Engineering and Management, University of Twente, NL

[3]Department of Physical Geography, Utrecht University, NL

Contents of this file

1. Text S1 to S2
2. Figures S1 to S8

Introduction

These Supplementary Materials contain a detailed description of the BRIE-D model (Text S1), as well as the dependence on significant wave height and SLR scenarios (taking constant rates or RCP scenarios) of the barrier system (Text S2).

Corresponding author: Laura Portos-Amill. Water Engineering and Management, University of Twente, 7500 AE, Enschede, The Netherlands (l.portosamill@utwente.nl).

Text S1.

1. Model Domain

The main asset of the model lies in describing the system by three separate regions in the cross-shore dimension: the active shoreface, the subaerial portion of the barrier island and the back-barrier lagoon (see Figure S1). We define the system in the cross-shore direction by the boundaries between these regions: the toe of the shoreface, the shoreline and the back-barrier shoreline.

The toe of the shoreface is located at $x = x_t$ and $z = \xi(t) - D_t$, where $\xi(t)$ is the sea level elevation at time t and

$$D_t = 8.9H_s \tag{1}$$

is the depth of closure, which depends on the long-term average offshore significant wave height H_s (Houston, 1995). The seaward shoreline of the barrier island is located at $x = x_s$ and $z = \xi(t)$, and the shoreline on the back-barrier side is located at $x = x_b$ and $z = \xi(t)$. We consider the subaerial portion of the barrier to be delimited by vertical profiles at both sides. The height of the subaerial portion of the barrier is denoted by H. The width of the barrier is defined as $W_b = x_b - x_s$. Note that all variables defined so far (except for mean sea level) depend on the alongshore direction as well. The back-barrier lagoon has a flat bottom and the shoreface is defined by a linear profile with slope $s_{sf} = D_t/(x_s - x_t)$.

The model is driven by tides (with a prescribed range), rate of SLR and waves that propagate from deep water toward the barrier, among other boundary conditions (e.g., shoreface slope). The waves are characterized by a significant wave height (assumed to be constant) and by an angle of incidence with respect to the $y-$axis. This angle is a stochastic variable that is determined by a probability density distribution that depends on

wave asymmetry (fraction of waves approaching from the left, looking offshore) and wave highness (fraction of waves approaching at a high angle, i.e., $|\phi_0| > 45°$, see Figure S1a).

2. Cross-shore Dynamics

There are three main cross-shore processes affecting the boundaries of the system and the barrier height: sediment transport on the shoreface, passive flooding due to SLR and overwash. We implement them in the BRIE-D model by considering the separate effects of each one of them on the three different boundaries, yielding

$$\frac{\partial x_t}{\partial t} = F_{t,sf} + F_{t,SL} \ , \tag{2}$$

$$\frac{\partial x_s}{\partial t} = F_{s,lt} + F_{s,sf} + F_{s,ow} + F_{s,sd} \ , \tag{3}$$

$$\frac{\partial x_b}{\partial t} = F_{b,ow} + F_{b,form} + F_{b,sd} + F_{b,Esc} \ , \tag{4}$$

$$\frac{\partial H}{\partial t} = F_{H,SL} + F_{H,ow} \ , \tag{5}$$

where *sf* stands for shoreface processes, *SL* for passive flooding due to SLR, and *ow* for overwash. These processes will be explained in this section. Furthermore, there are non cross-shore processes affecting these boundaries as well, *form* stands for inlet formation, *sd* stands for sediment distribution in the inlet, *Esc* for sediment exchange between the inlet and the flood-tidal delta (which is partly parameterized following the theory by Escoffier, 1940) and $F_{s,lt}$ is the contribution due to alongshore gradients in the littoral drift. These three processes are explained in Sections 3, 5, 6 and 8, respectively.

2.1. Shoreface Transport

We compute the shoreface transport based on the deviations from an equilibrium slope $s_{sf,eq}$, which is defined by the balance between onshore sediment transport by waves and

the offshore directed transport due to gravity. These deviations result in the shoreface transport

$$Q_{sf} = k_{sf}(s_{sf,eq} - s_{sf}) \ , \tag{6}$$

which is controlled by the shoreface response rate k_{sf}. By imposing mass conservation of sediment, it follows that the evolution of x_s and of x_t due to the sole effect of Q_{sf} is given by

$$F_{s,sf} = -4Q_{sf}\frac{H + D_t}{(2H + D_t)^2} \ , \tag{7}$$

$$F_{t,sf} = 4Q_{sf}\frac{H + D_t}{D_t(2H + D_t)} \ . \tag{8}$$

The shoreface response rate represents the integrated cross-shore sediment transport between the depth of closure and the wave breaking depth. We adopt the expression for k_{sf} obtained by Nienhuis and Lorenzo-Trueba (2019),

$$k_{sf} = \frac{e_s c_s g^{11/4} H_s^5 T_p^{5/2}}{960 R \pi^{7/2} w_s^2}\left(\frac{\frac{1}{\frac{11}{4}z_0^{11/4}} - \frac{1}{\frac{11}{4}D_t^{11/4}}}{D_t - z_0}\right) \ , \tag{9}$$

in units of $\mathrm{m^3 m^{-1} s^{-1}}$. In this expression, e_s is the suspended sediment transport efficiency factor, c_s is the friction factor, g is the gravitational acceleration, T_p is the peak wave period, R is the submerged specific gravity of sediment, w_s is the sediment settling velocity and z_0 depth where waves break. Following Lorenzo-Trueba and Ashton (2014), the equilibrium slope is given by

$$s_{sf,eq} = \frac{3w_s}{4\sqrt{gD_t}}\left(5 + \frac{3T_p^2 g}{4\pi^2 D_t}\right) \ . \tag{10}$$

Here, the sediment settling velocity is computed based on the empirical formulation developed by Ferguson and Church (2004),

$$w_s = \frac{RgD_{50}^2}{\alpha + \sqrt{\frac{3}{4}RgD_{50}^3}} \ , \tag{11}$$

where $\alpha = 18 \cdot 10^{-6}$ m^2/s.

2.2. Passive Flooding by SLR

SLR causes passive flooding, apart from sediment transport and overwash. In the BRIE-D model, inundation results in reduction of the barrier height, landward translation of the toe of the shoreface and shoreface steepening. Imposing conservation of sediment of the entire barrier system, the rates of change of the position of the toe of the shoreface and barrier height that are solely due to flooding are described by

$$F_{t,SL} = \frac{2\dot{\xi}}{s_{sf}} \ , \tag{12}$$

$$F_{H,SL} = -\dot{\xi} \ , \tag{13}$$

where $\dot{\xi}$ represents the rate of SLR.

2.3. Overwash

During storms, waves transport sand from the ocean side of the barrier and deposit it on the barrier or along its landward margin, resulting in landward migration of the barrier. We model this behavior by removing sediment from the upper part of the shoreface, keeping the toe of the shoreface constant and shifting the shoreline position landward at a rate

$$F_{s,ow} = \frac{2Q_{ow}}{(2H + D_t)(1 - f)} \ . \tag{14}$$

This expression is for a given overwash transport Q_{ow}, to be specified later, where the $(1 - f)$ factor accounts for fine-grained sediment deposition in the back barrier. Sediment deposition can take place on top of the barrier, resulting in subaerial barrier elevation, or on the back barrier, resulting in landward migration of the back-barrier shoreline such

that

$$F_{b,ow} = \frac{Q_{ow,b}}{H + D_{lagoon}} \ , \tag{15}$$

$$F_{H,ow} = \frac{Q_{ow,h}}{W_b} \ , \tag{16}$$

with

$$Q_{ow} = Q_{ow,h} + Q_{ow,b} \ . \tag{17}$$

The depth D_{lagoon} in Equation 15 corresponds to that of the back-barrier basin. The overwash transports are computed based on the barrier deficit volume per unit length V_d, which represents the difference, for a given shoreline location, between a current barrier configuration and one that is both high and wide enough such that overwash is presumed not to occur. This volume per unit length has both top barrier $V_{d,h}$ and back-barrier $V_{d,b}$ components,

$$V_d = V_{d,h} + V_{d,b} \ , \tag{18}$$

with

$$V_{d,h} = \max[0, (H_{crit} - H)W_b] \ , \tag{19}$$

$$V_{d,b} = \max[0, (W_{b,crit} - W_b)(H + D_{lagoon})] \ . \tag{20}$$

When the barrier width and height are below their critical values, the overwash transports $Q_{ow,b}$ and $Q_{ow,h}$ scale with their associated deficit volumes. This results in an overwash transport heightening the barrier,

$$Q_{ow,h} = Q_{ow,max} \frac{V_{d,h}}{\max(V_{d,b} + V_{d,h}, H_{crit} W_{b,crit})} \ , \tag{21}$$

and an overwash transport widening the barrier,

$$Q_{ow,h} = Q_{ow,max} \frac{V_{d,b}}{\max(V_{d,b} + V_{d,h}, H_{crit} W_{b,crit})} \ . \tag{22}$$

The maximum overwash transport $Q_{ow,max}$ depends on storm frequency and magnitude, as well as local sediment characteristics. Lorenzo-Trueba and Ashton (2014) found that it has values in the range $10^{-8} - 10^{-6}$ $\mathrm{m^3m^{-1}s^{-1}}$ (i.e. $\sim 1 - 100$ $\mathrm{m^3m^{-1}yr^{-1}}$).

3. Inlet Formation

There are two processes by which inlets form: breaching and drowning. Inlets can form every T_{storm} years, at a location lying at least 5 km from existing inlets and with minimum barrier volume per unit length, computed as $W_b H$. In this formulation T_{storm} represents a storm return period, taken as $T_{storm} = 10$ yr. The initial width of a breached inlet is set to 1 km, and its depth is computed assuming an aspect ratio γ_{aspect} such that $D_{inlet} = \gamma_{aspect} W_{inlet}$, where D_{inlet} and W_{inlet} stand for inlet depth and width, respectively. The inlet aspect ratio is assumed to be constant only for small inlets. Based on observations (Hume & Herdendorf, 1992), we set the maximum inlet depth to be 15 m, above which an increase in inlet cross-sectional area causes an increases in only inlet width.

Inlets can also form due to barrier drowning, that is if the top of the barrier is below MSL or if the barrier width becomes negative. Lorenzo-Trueba and Ashton (2014) defined these situations as height and width drowning, respectively. Note that in the case of height or width drowning, Equations 3, 4 and 5 still apply, even if the subaerial part of the barrier has disappeared. In these cases, inlets form independently of their distance to pre-existing inlets and their width is computed as the alongshore extent over which W_b and/or H are negative. Inlet depth is computed, with the assumption that the aspect ratio is the same as for breached inlets. This means that, in the case of height drowning, the inlet ends up being deeper than the initial depth of the drowned portion. To make up for that, the corresponding inlet volume ($W_b W_{inlet}(H + D_{inlet})$) is placed in the flood-tidal delta by

increasing the back-barrier location by

$$F_{b,form} = \frac{dW_b}{dt}\left(\frac{H + D_{inlet}}{D_{lagoon}}\right) \ . \tag{23}$$

The same procedure is applied for breached inlets.

After formation, we let the cross-sectional area of an inlet, A_{inlet}, evolve depending on the different sources or sinks of sediment,

$$\frac{dA_{inlet}}{dt} = G_{sd} + G_{Esc} + G_m + G_d \ , \tag{24}$$

where d represents the variations due to barrier drowning and m, those due to merging with pre-existing inlets. Expressions of the terms on the right hand side will be given in Sections 5, 6.

4. Alongshore Transport into Inlets

The barrier is interrupted in the alongshore direction by inlets, whose dynamics are controlled by the alongshore sediment transport (also known as littoral drift) Q_s they receive (see Figure S2). THE alongshore sediment transport along the barrier islands is computed by applying the CERC formula, the same way as it is done in the BRIE model,

$$Q_s = kH_s^{12/5}T_p^{1/5}\cos^{6/5}(\phi_0 - \theta)\sin(\phi_0 - \theta) \ . \tag{25}$$

In this expression k is a constant that ~ 0.06 $\mathrm{m^{3/5}s^{-6/5}}$ (Nienhuis et al., 2015), and ϕ_0 is the wave direction. The wave height at breaking H_b that is in the original CERC formula is converted to H_s using Snell's refraction law and conservation of wave energy (Ashton & Murray, 2006). The orientation of the shoreline θ is defined by $\tan\theta = \partial x_s/\partial y$ and may have a different value for each inlet. Note that Q_s has units of $\mathrm{m^3\ s^{-1}}$, not $\mathrm{m^3\ m^{-1}\ s^{-1}}$, as it is the case for Q_{sf} and Q_{ow}.

At every time step, the wave direction ϕ_0 is computed from a cumulative distribution function defined by wave asymmetry (a, corresponding to the fraction of waves approaching from the left looking offshore, i.e. $\phi_0 > 0$) and wave highness (h, corresponding to the fraction of high angle waves, i.e. $|\phi_0| > 45$). The probability density function is defined as

$$P(\phi_0) = \begin{cases} P_1 = (4/\pi)ah & \text{if } -\frac{\pi}{2} < \phi_0 < -\frac{\pi}{4} \\ P_2 = (4/\pi)a(1-h) & \text{if } -\frac{\pi}{4} < \phi_0 < 0 \\ P_3 = (4/\pi)(1-h)(1-a) & \text{if } 0 < \phi_0 < \frac{\pi}{4} \\ P_4 = (4/\pi)(1-a)h & \text{if } \frac{\pi}{4} < \phi_0 < \frac{\pi}{2} \end{cases}, \tag{26}$$

where $\sum_{i=1}^{4} P_i \frac{\pi}{4} = 1$ (Nienhuis & Lorenzo-Trueba, 2019; Ashton & Murray, 2006). Then, for a given random number G uniformly distributed between 0 and 1, the angle ϕ_0 is computed as

$$\phi_0 = \begin{cases} -\frac{\pi}{2} + \frac{G}{P_1} & \text{if } G \leq P_1 \frac{\pi}{4} \\ -\frac{\pi}{4} + \frac{G - P_1\pi/4}{P_2} & \text{if } P_1\frac{\pi}{4} \leq G \leq (P_1+P_2)\frac{\pi}{4} \\ \frac{G-(P_1+P_2)\pi/4}{P_3} & \text{if } (P_1+P_2)\frac{\pi}{4} \leq G \leq (P_1+P_2+P_3)\frac{\pi}{4} \\ \frac{\pi}{4} + \frac{G-(P_1+P_2+P_3)\pi/4}{P_4} & \text{if } (P_1+P_2+P_3)\frac{\pi}{4} \leq G \leq 1 \end{cases}. \tag{27}$$

5. Inlet Migration and Sediment Deposition at the Flood Delta

Sediment is distributed around the inlet in terms of fractions of the littoral drift Q_s that occurs at the end of the updrift barrier island. A fraction β of the littoral drift is bypassed to the downdrift side of the barrier, a fraction δ is deposited on the flood-tidal delta and the remaining part (a fraction α) is deposited on the updrift tip of the barrier (see the blue arrows in Figure S2). Conservation of sediment mass implies that α, β and δ sum up to 1. Additionally, erosion of sediment occurs at the downdrift tip of the barrier. Part of this sediment continues to move downdrift into the littoral zone at a rate $\beta_r Q_s$, part of it is deposited on the flood tidal delta at a rate $\delta_r Q_s$, or is deposited on the updrift tip of the barrier at a rate $\alpha_r Q_s$ (see the red arrows in Figure S2). Expressions for all fractions,

in terms of tidal current, wave climate, inlet width and barrier width, were obtained using Delft3D experiments (Nienhuis & Ashton, 2016).

The amount of sediment deposited on the updrift side defines the inlet migration rate,

$$\frac{dy_{inlet}}{dt} = \frac{Q_s(\alpha + \alpha_r)}{A_{b,up}} \ , \tag{28}$$

where $A_{b,up}$ is the cross-sectional area of the barrier updrift of the inlet, $W_b(D_{inlet} + H)$. Inlet migration creates the new barrier at mean sea level. The deficit (excess) in alongshore sediment transport in the downdrift side (i.e. it being $(\beta+\beta_r)Q_s$ instead of Q_s) is balanced taking sediment from (adding it to) the downdrift side of the barrier, resulting in a change per time in the position of the seaward shoreline

$$F_{s,sd} = \frac{(1 - \beta - \beta_r)Q_s}{(H + D_{lagoon})W_{inlet}} \ , \tag{29}$$

such that the alongshore sediment transport received by each inlet equals Q_s.

The sediment distribution leads to a change in the location of the back-barrier shoreline,

$$F_{b,sd} = \frac{Q_s(\delta + \delta_r)}{W_{inlet}D_{lagoon}} \ . \tag{30}$$

This represents deposition of sediment at the flood delta because we define the flood-tidal delta volume to be dependent on the position of the back-barrier shoreline,

$$V_{fld} = (W_b + W_{b,crit})W_{inlet}D_{lagoon} \ , \tag{31}$$

which depends on the critical barrier width $W_{b,crit} = 200$ m, such that it is never zero. Here $W_b = x_b - x_s$ is the width of the barrier, which depends on the position of the back-barrier shoreline x_b.

Likewise, the sediment distribution within the inlet causes evolution of the cross-sectional area of the inlet,

$$G_{sd} = D_{inlet}\left(\frac{1}{A_{b,down}}\frac{dV_{down}}{dt} - \frac{1}{A_{b,up}}\frac{dV_{up}}{dt}\right) , \tag{32}$$

where the changes in downdrift and updrift volumes are respectively defined by

$$\frac{dV_{down}}{dt} = Q_s(\alpha_r + \beta_r + \delta_r) , \quad \frac{dV_{up}}{dt} = Q_s(\alpha + \alpha_r) . \tag{33}$$

The parametrizations used for the distribution of littoral drift over the different parts of the barrier system, α, β, δ, α_r, β_r and δ_r, depend on the nondimensional inlet momentum balance I as (Nienhuis & Ashton, 2016, see Figure S3a)

$$\beta = \frac{1}{1 + 10I^{-3}} , \quad \beta_r = \frac{0.9}{1 + 0.9I^{-3}} , \tag{34}$$

$$\delta = \frac{1}{1 + 3I^{-3}} , \quad \delta_r = 0.03 + \frac{0.57}{1 + 3I^{-3}} , \tag{35}$$

$$\alpha = 1 - \beta - \delta , \quad \alpha_r = 0.6\alpha . \tag{36}$$

Here, I is defined as the ratio between the tidal and wave momentum flux, M_t and M_w,

$$M_t = \rho_w u_e^2 A_{inlet} , \quad M_w = S_{xy} W_{inlet} , \tag{37}$$

in which ρ_w is the density of water. The expression for M_w contains S_{xy}, which is the wave averaged, depth integrated transfer of y-momentum in the x direction that is solely due to waves (Longuet-Higgins & Stewart, 1962),

$$S_{xy} = E(c_g/c)\cos(\phi_0)\sin(\phi_0) , \tag{38}$$

with E being the mean depth-integrated wave energy density,

$$E = \frac{1}{16}\rho_w g H_s^2 . \tag{39}$$

Combining these results yields

$$I = \nu \frac{M_t}{M_w} \frac{W_{inlet}}{W_b} = \nu \frac{\rho_w U_e^2 A_{inlet}}{\frac{1}{16}\rho_w g H_s^2 W_{inlet}} \frac{W_{inlet}}{W_b} \ , \tag{40}$$

where U_e is the equilibrium velocity amplitude through the inlet ($U_e = 1$ m/s) and ν is a dimensionless parameter, which is set at 0.02.

The definition of the sediment transport eroded from the downdrift tip and deposited into the flood tidal delta (δ_r) used in the BRIE-D model differs from that used in the BRIE model. In the BRIE model, it was set such that the inlet width remained unchanged. Here, this constraint is released by making δ_r dependent on I, following the relation found by Nienhuis and Ashton (2016). This change in formulation is more physical, because it allows for both tips of the barrier to be disconnected. Its consequence is that it causes more sediment to be deposited on the flood-tidal delta in BRIE-D compared to BRIE, because δ_r is always positive. In contrast, δ_r takes mostly negative values in the BRIE model (meaning that sediment is transported from the flood-tidal delta to the downdrift tip of the barrier).

A positive feedback resulting in inlet growth can arise in BRIE-D because of this new relation between inlet bank erosion and the inlet momentum balance. Inlets tend to widen and the barrier tends to narrow under drowning situations. A wider inlet and a narrower barrier cause a larger value for the inlet momentum balance I, which corresponds to more sediment being deposited into the flood-tidal delta (due to larger δ and δ_r). Overall, the BRIE-D model exhibits a larger deposition into the flood-tidal delta than that of the BRIE model. We set a maximum value for the flood-tidal delta beyond which the nondimensional inlet momentum balance I is set to 0.1 (causing a very low deposition into the flood-tidal delta, defined by δ and δ_r). This threshold in V_{fld} prevents unrealistic

values for the flood-tidal delta volume, and is parameterized the same way as it is done in the BRIE model, following empirical data from Powell, Thieke, and Mehta (2006), yielding

$$V_{fld,max} = V_{ref} \left[\frac{U A_{inlet}/(2\omega)}{V_{ref}} \right]^{0.37} , \tag{41}$$

with $V_{ref} = (1 \cdot 10^4)^{1/0.63}$ m^3 $= 2.235 \cdot 10^6$ m^3. Furthermore, we scale the nondimensional inlet momentum balance I by a factor $\nu = 0.02$ (see Equation 40). As a result of this modification, the larger deposition in the flood-tidal delta (due to wider inlets, narrower barrier and the new parametrization for δ_r) is counteracted. Therefore, we obtain a more realistic evolution of the flood-tidal delta volume, as well as the other parameters involved.

6. Variations in the Cross-sectional Area of the Inlet

We depart from the formulation given in Nienhuis and Lorenzo-Trueba (2019) by allowing for variations in the cross-sectional area of the inlet. Apart from the variations caused by the difference in deposition of littoral drift on the downdrift and updrift barrier (Equation 32), we also include variations in the cross-sectional area of the inlet depending on the balance in sediment exchange with the flood-tidal delta. This balance depends on a prescribed transport from the flood-tidal delta to the inlet and the export of sediment from the inlet to the flood-tidal delta due to tidal currents. The latter is parameterized following the concepts by Escoffier (1940), and the formulations given in van de Kreeke (2004), yielding

$$W_b \frac{dA_{Esc}}{dt} = -M + S , \tag{42}$$

where M is the sediment imported into the inlet from the flood-tidal delta and S is the transport capacity of the flood-tidal current, which is parameterized as

$$S = \kappa U^2 \ , \tag{43}$$

with U the tidal current amplitude in the inlet. In equilibrium, $U = U_e$ and A_{Esc} is constant, so $\kappa = M/U_e^2$. This allows the right-hand side of Equation 42 to be expressed in terms of M, U and U_e , yielding

$$G_{Esc} = \frac{dA_{Esc}}{dt} = -\frac{M}{W_b}\left(1 - \left(\frac{U}{U_e}\right)^2\right) \ . \tag{44}$$

We obtain the tidal velocity amplitude U from the inlet hydrodynamic equations presented in Brown (1928) and summarized in de Swart and Zimmerman (2009), assuming that both the length of the inlet and the size of the bay are short compared with the tidal wavelength.

It is assumed that the cross-sectionally averaged tidal velocity u is spatially uniform in the inlet, and that the sea surface η is spatially uniform in the back-barrier lagoon. Tidal forcing is imposed at the seaward side, $\eta_0 = a_0 \sin(\omega t)$, where η_0 is the offshore sea surface elevation, a_0 is the tidal amplitude and ω is the tidal radial frequency. Integrating the momentum equation over the inlet, we obtain

$$W_b \frac{du}{dt} = -g(\eta - \eta_0) - \frac{8}{3\pi} c_d \frac{U}{D_{inlet}} u W_b \ , \tag{45}$$

where g is the gravitational acceleration. Here, the quadratic stress $c_d|u|u$ is linearized, by projecting it onto the harmonic component that oscillates with ω, and U is the amplitude of u. Likewise, integrating the continuity equation over the back-barrier lagoon yields

$$(1 - f_{marsh}) A_{lagoon} \frac{d\eta}{dt} = u A_{inlet} \ , \tag{46}$$

where the factor f_{marsh} is the fraction of the back-barrier lagoon surface area (A_{lagoon}) covered by marsh, thus not contributing to the tidal prism. By taking the time derivative of Equation 45 and subsequently using Equation 46 to eliminate η it follows a single differential equation for the velocity u:

$$\frac{d^2u}{dt^2} + \frac{8}{3\pi}c_d\frac{U}{D_{inlet}}\frac{du}{dt} = -\frac{g}{W_b}\frac{A_{inlet}}{(1-f_{marsh})A_{lagoon}}u + \frac{g}{W_b}\frac{d\eta_0}{dt} \ . \tag{47}$$

Assuming a nontransient solution of the form

$$u = \mathrm{Re}\left(\hat{U}e^{-i\omega t}\right) \ , \quad |\hat{U}| = U \ , \tag{48}$$

and substituting

$$\frac{d\eta_0}{dt} = \mathrm{Re}\left(a_0\omega e^{-i\omega t}\right) \ , \tag{49}$$

into Equation 47 yields

$$-\omega^2\hat{U} - i\frac{8}{3\pi}\frac{c_d}{D_{inlet}}\omega U\hat{U} = -\frac{g}{W_b}\frac{A_{inlet}}{(1-f_{marsh})A_{lagoon}}\hat{U} + \frac{g}{W_b}a_0\omega \ . \tag{50}$$

Here, we define the Helmholtz frequency,

$$\omega_H^2 = \frac{g}{W_b}\frac{A_{inlet}}{(1-f_{marsh})A_{lagoon}} \ , \tag{51}$$

and

$$\lambda = \frac{8}{3\pi}\frac{c_d}{D_{inlet}}\omega \ . \tag{52}$$

Rearranging Equation 50 yields

$$\left[\left(-\omega^2 + \omega_H^2\right) - i\lambda U\right]\hat{U} = \frac{g}{W_b}a_0\omega \ . \tag{53}$$

Taking the absolute value and the square of this expression, it follows

$$\left[\left(-\omega^2 + \omega_H^2\right)^2 + \lambda^2U^2\right]U^2 = \left(\frac{g}{W_b}a_0\omega\right)^2 \ , \tag{54}$$

or

$$aU^4 + bU^2 + c = 0 \ , \tag{55}$$

with

$$a = \lambda^2 \ , \quad b = (-\omega^2 + \omega_H^2)^2 \ , \quad c = -\left(\frac{g}{W_b} a_0 \omega\right)^2 \ . \tag{56}$$

The solution that yields $U \geq 0$ is

$$U = \left[\frac{-b + \sqrt{b^2 - 4ac}}{2a}\right]^{1/2} \ . \tag{57}$$

In this formulation, the friction coefficient and the marsh cover depend on the flood-tidal delta volume,

$$c_d = \frac{gn^2}{D_{inlet}^{1/3}} + \frac{D_{inlet}}{W_b} \frac{V_{fld}}{V_{fld,max}} \ , \quad f_{marsh} = 0.5 + 0.4 \frac{V_{fld}}{V_{fld,max}} \ , \tag{58}$$

where n is the Manning roughness coefficient, taken as $n = 0.05$ s m$^{-1/3}$. This formulation for the bottom friction includes the effects of head loss due to flow separation (second term, see Terra et al., 2005, and references therein). The dependence of both the friction coefficient and the marsh cover on the flood-tidal delta volume prevents unrealistically large values for the amplitude of the tidal velocity in the inlet, which caused abrupt changes in the cross-sectional area of the inlet.

The sediment gained (lost) by the inlet due to these dynamics (Equation 44) is taken from (given to) the flood-tidal delta (see the green arrows in Figure S2) causing a change in the back-barrier shoreline along the inlet width

$$F_{b,Esc} = -\frac{M}{W_b} \left(1 - \left(\frac{U}{U_e}\right)^2\right) \frac{W_b}{D_{lagoon} W_{inlet}} \ . \tag{59}$$

Note that the flood-tidal delta volume depends on the position of the back-barrier shoreline (Equation 31).

A third way inlets can increase their cross-sectional area is by merging with other inlets. The increase in the cross-sectional area of the inlet due to merging with other inlets G_m is such that the total cross-sectional area is conserved. As a result, if inlets j and k merge, with $j < k$, the cross-sectional area of inlet j is then $A_{inlet,j} + A_{inlet,k}$, and inlet k is no longer present at the next time step.

Lastly, the increase in the cross-sectional area of the inlet due to barrier drowning depends on the length of the portion of the barrier that drowned, denoted as W_d, which is either due to negative barrier width or negative barrier height,

$$G_d = \frac{dW_d}{dt}\ \gamma_{aspect} W_d\ , \tag{60}$$

where the corresponding depth is computed using the inlet aspect ratio γ_{aspect} ($\gamma_{aspect} = D_{inlet}/W_{inlet}$).

7. Equilibrium cross-sectional area

The BRIE-D model is also able to compute the hypothetical cross-sectional area that an inlet would have if it were to be in equilibrium. That corresponds to the cross-sectional area that the inlet would instantaneously attain in the BRIE model. Given the environment characteristics, the equilibrium cross-sectional area is computed analytically from the inlet area-velocity relationship (Escoffier, 1940; de Swart & Zimmerman, 2009), yielding

$$A_{inlet} = \omega(1 - f_{marsh}) L_{lagoon} W_{lagoon} \sqrt{g a_0}\, \tilde{A}_{inlet}\ , \tag{61}$$

with

$$\tilde{A}_{inlet} = \frac{2\tilde{A}_H}{3} + \frac{2^{2/3} F_0}{6} + \frac{2^{1/3}\left(3 + \tilde{A}_H^2 \tilde{u}_e^2\right)}{3\tilde{u}_e^2 F_0}\ . \tag{62}$$

Here, $\tilde{A}_H = \omega W_b/\sqrt{ga_0}$ is a resonance nondimensional cross-sectional area, $\tilde{u}_e = U_e/\sqrt{ga_0}$ is a nondimensional equilibrium velocity, and F_0 is defined as

$$F_0 = \left(6\sqrt{3}\sqrt{\tilde{A}_H^3\tilde{\gamma}^{-2}\tilde{u}_e^{-2} - \tilde{A}_H^4\tilde{u}_e^{-2} + 2\tilde{A}_H^2\tilde{u}_e^{-4} - 9\tilde{A}_H\tilde{\gamma}^{-2} - \tilde{u}_e^{-6} + \frac{27}{4}\tilde{\gamma}^{-4}\tilde{u}_e^{-4}} \right. \\ \left. -27\tilde{\gamma}^{-2}\tilde{u}_e^2 - 2\tilde{A}_H^3 + 18\tilde{A}_H\tilde{u}_e^{-2} \right)^{1/3} , \tag{63}$$

where $\tilde{\gamma}$ is the ratio of the potential tidal prism and the inlet friction,

$$\tilde{\gamma} = \frac{\gamma_{aspect}\sqrt{\omega L_{lagoon} W_{lagoon}(1 - f_{marsh})\sqrt{a_0/g}}}{\frac{8}{3\pi}c_d W_b} . \tag{64}$$

Here, W_{lagoon} and L_{lagoon} are the cross-shore width of the lagoon and the alongshore length of the lagoon draining to a particular tidal inlet, respectively.

8. Evolution of the Shoreline

The evolution of the shoreline is given by the equation

$$\frac{\partial x_s}{\partial t} = -\frac{1}{D_t + H}\frac{\partial Q_s}{\partial y} + \frac{\partial x_{s,ext}}{\partial t} , \tag{65}$$

where Q_s is the alongshore sediment transport, and the last term in the right hand side accounts for cross-shore sediment transport due to shoreface processes, overwash and sediment distribution around the inlet,

$$\frac{\partial x_{s,ext}}{\partial t} = F_{s,sf} + F_{s,ow} + F_{s,sd} . \tag{66}$$

Here, it is assumed that Q_s is given by the CERC formula (Equation 25). In our model, the only term of Q_s depending on y is the shoreline orientation θ, with

$$\tan\theta = \frac{\partial x_s}{\partial y} . \tag{67}$$

So

$$\frac{\partial Q_s}{\partial y} = \frac{\partial Q}{\partial \theta}\frac{\partial \theta}{\partial y} \tag{68}$$

and

$$\frac{\partial Q_s}{\partial \theta} = kH_s^{12/5}T_p^{1/5}\cos^{1/5}(\phi_0-\theta)\left(\frac{6}{5}\sin^2(\phi_0-\theta)-\cos^2(\phi_0-\theta)\right) \ . \tag{69}$$

For small angles θ, it follows that

$$\frac{\partial \theta}{\partial y} \simeq \frac{\partial}{\partial y}\tan\theta = \frac{\partial}{\partial y}\frac{\partial x_s}{\partial y} = \frac{\partial^2 x_s}{\partial y^2} \ , \tag{70}$$

yielding,

$$\frac{\partial Q_s}{\partial y} = kH_s^{12/5}T_p^{1/5}\cos^{1/5}(\phi_0-\theta)\left(\cos^2(\phi_0-\theta)-\frac{6}{5}\sin^2(\phi_0-\theta)\right)\frac{\partial^2 x_s}{\partial y^2} \ . \tag{71}$$

The shoreline diffusivity D is defined by convolving the angular dependence of the diffusive term in Equation 71 with the probability distribution in Equation 26 in order to generate a diffusivity representative of the long-term average wave climate,

$$D = \frac{k}{(H+D_t)}H_s^{12/5}T_p^{1/5}\cos^{1/5}(\phi_0-\theta)\left(\cos^2(\phi_0-\theta)-\frac{6}{5}\sin^2(\phi_0-\theta)\right)P(\phi_0) \ , \tag{72}$$

yielding

$$\frac{\partial x_s}{\partial t} = D\frac{\partial^2 x_s}{\partial y^2} + F_{s,sf} + F_{s,ow} + F_{s,sd} \ . \tag{73}$$

Note that D may become negative, yielding a high-angle wave instability (Ashton et al., 2001).

9. Initial and Boundary Conditions

Simulations are initialized with a barrier without inlets. The position of the seaward shoreline $x = x_s$ is computed imposing the equilibrium shoreface slope between $x = x_t$ and $x = x_s$ and adding a random perturbation following a uniform distribution between 0 and 1 m. The back-barrier shoreline is set such that the barrier width equals 200 m. The barrier height is set to 2 m. These are representative values for barrier width and height

(Mulhern et al., 2017; Leatherman, 1983). We apply periodic boundary conditions in the alongshore direction.

10. Numerical Implementation

At each time step, we add all contributions to changes in x_t, x_b, A_{inlet} and H and we solve their respective differential equations using an Euler forward method taking a time step $\Delta t = 0.05$ yr ($\sim$ 18 days). We solve Equation 73 for x_s using a Crank-Nicolson scheme (Crank & Nicolson, 1947), where we apply periodic boundary conditions in the alongshore direction (Nienhuis & Lorenzo-Trueba, 2019). The alongshore extent of the domain covers 50 km with a grid size is taken as $\Delta y = 100$ m.

Text S2.

Figures S4 and S5 show the alongshore fraction of the barrier lying below MSL that is computed from the actual evolution of the barrier and assuming an equilibrium situation, respectively. Note the differences at years 300 and 500 for higher rates of SLR and wave heights. Situations depicted in white represent simulations that became unstable while drowning and stopped before the year 500.

Simulations performed with the scenarios RCP2.6, RCP4.5 and RCP8.5 show the same qualitative behavior as those with constant rates of SLR (see Figures S6, S7, S8). Note that approximate equivalences can be made in terms of MSL between the three RCP scenarios and the constant rates of SLR $\xi = 5$, 6, 10 mm/yr, respectively.

References

Ashton, A. D., & Murray, A. B. (2006). High-angle wave instability and emergent shoreline shapes: 1. Modeling of sand waves, flying spits, and capes. *Journal of*

Geophysical Research: Earth Surface, *111*(F4). doi: 10.1029/2005JF000422

Ashton, A. D., Murray, A. B., & Arnoult, O. (2001). Formation of coastline features by large-scale instabilities induced by high-angle waves. *Nature*, *414*, 296-300. doi: 10.1038/35104541

Brown, E. I. (1928). Inlets on sandy coasts. In *Proceedings of the American Society of Civil Engineers* (Vol. 54, pp. 505–554).

Crank, J., & Nicolson, P. (1947). A practical method for numerical evaluation of solutions of partial differential equations of the heat-conduction type. *Mathematical Proceedings of the Cambridge Philosophical Society*, *43*(1), 50–67.

de Swart, H., & Zimmerman, J. (2009). Morphodynamics of tidal inlet systems. *Annual Review of Fluid Mechanics*, *41*(1), 203-229. doi: 10.1146/annurev.fluid.010908.165159

Escoffier, F. (1940). The stability of tidal inlets. *Shore and Beach*(8), 114-115.

Ferguson, R., & Church, M. (2004, 11). A simple universal equation for grain settling velocity. *Journal of Sedimentary Research*, *74*(6), 933-937. doi: 10.1306/051204740933

Houston, J. (1995). Beach-fill volume required to produce specified dry beach width. In *Coastal Engineering Technical Note* (p. 11-32). US Army Engineer Waterways Experiment Station Vicksburg, Mississippi.

Hume, T. M., & Herdendorf, C. E. (1992). Factors controlling tidal inlet characteristics on low drift coasts. *Journal of Coastal Research*, *8*(2), 355–375.

Leatherman, S. P. (1983). Barrier dynamics and landward migration with Holocene sea-level rise. *Nature*, *301*(5899), 415–417.

Longuet-Higgins, M. S., & Stewart, R. (1962). Radiation stress and mass transport in

gravity waves, with application to 'surf beats'. *Journal of Fluid Mechanics*, *13*(4), 481–504.

Lorenzo-Trueba, J., & Ashton, A. D. (2014). Rollover, drowning, and discontinuous retreat: Distinct modes of barrier response to sea-level rise arising from a simple morphodynamic model. *Journal of Geophysical Research: Earth Surface*, *119*(4), 779-801. doi: 10.1002/2013JF002941

Mulhern, J. S., Johnson, C. L., & Martin, J. M. (2017). Is barrier island morphology a function of tidal and wave regime? *Marine Geology*, *387*, 74-84. doi: 10.1016/j.margeo.2017.02.016

Nienhuis, J. H., & Ashton, A. D. (2016). Mechanics and rates of tidal inlet migration: Modeling and application to natural examples. *Journal of Geophysical Research: Earth Surface*, *121*(11), 2118-2139. doi: 10.1002/2016JF004035

Nienhuis, J. H., Ashton, A. D., & Giosan, L. (2015). What makes a delta wave-dominated? *Geology*, *43*(6), 511-514. doi: 10.1130/G36518.1

Nienhuis, J. H., & Lorenzo-Trueba, J. (2019). Simulating barrier island response to sea level rise with the barrier island and inlet environment (BRIE) model v1.0. *Geoscientific Model Development*, *12*(9), 4013–4030. doi: 10.5194/gmd-12-4013-2019

Powell, M. A., Thieke, R. J., & Mehta, A. J. (2006). Morphodynamic relationships for ebb and flood delta volumes at Florida's tidal entrances. *Ocean Dynamics*, *56*(3), 295–307. doi: 10.1007/s10236-006-0064-3

Terra, G. M., van de Berg, W. J., & Maas, L. R. (2005). Experimental verification of Lorentz' linearization procedure for quadratic friction. *Fluid Dynamics Research*, *36*(3), 175-188. doi: 10.1016/j.fluiddyn.2005.01.005

van de Kreeke, J. (2004). Equilibrium and cross-sectional stability of tidal inlets: application to the Frisian Inlet before and after basin reduction. *Coastal Engineering*, *51*(5), 337-350. doi: 10.1016/j.coastaleng.2004.05.002

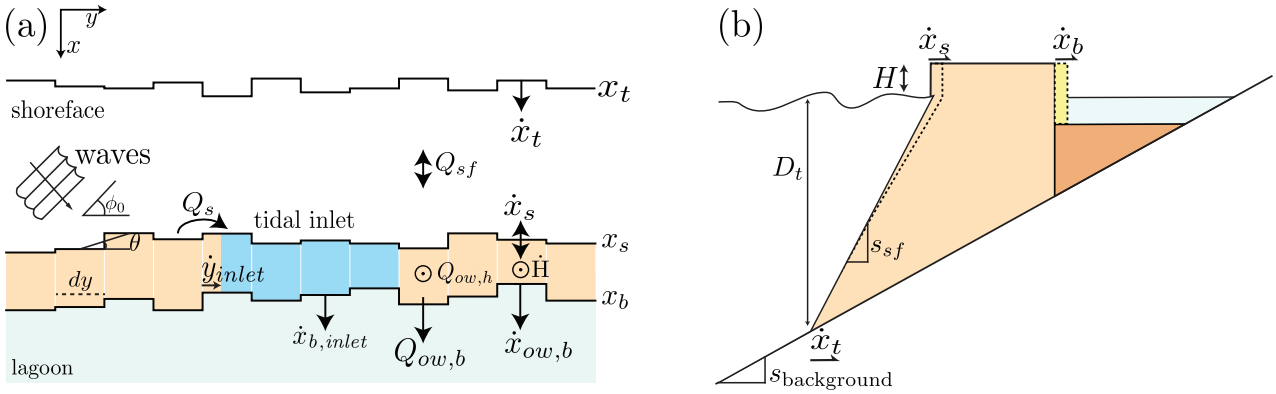

Figure S1. Schematized model domain: **(a)** plan view highlighting the three moving boundaries (toe of the shoreface x_t, shoreline x_s and back-barrier shoreline x_b) and barrier height H as well as the sediment transports determining their evolution. Vectors indicate the direction of potential changes, with the dot symbolizing barrier heightening. We use $\dot{x}$ to represent the local time derivative. **(b)** Cross-shore view of the barrier showing landward barrier migration in terms of $\dot{x}_s$ and $\dot{x}_b$. Modified from Nienhuis and Lorenzo-Trueba (2019).

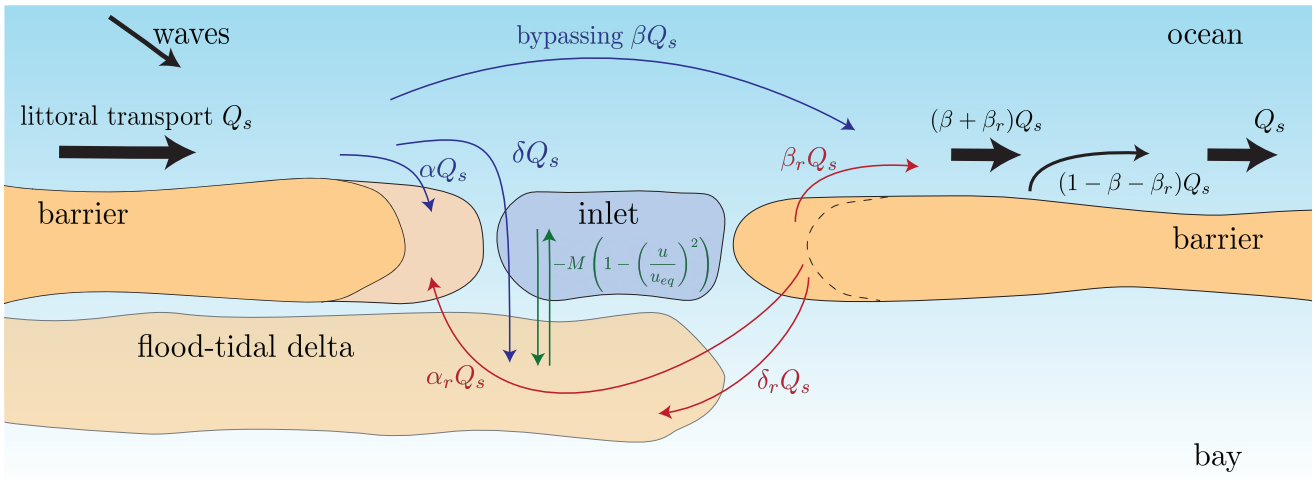

Figure S2. Mass balance box model defining inlet dynamics including sediment exchange with updrift and downdrift tips of the barrier, as well as with the flood-tidal delta. Note that the flood-tidal delta extends through the updrift barrier because it has been building up as the inlet was migrating. Modified from Nienhuis and Ashton (2016).

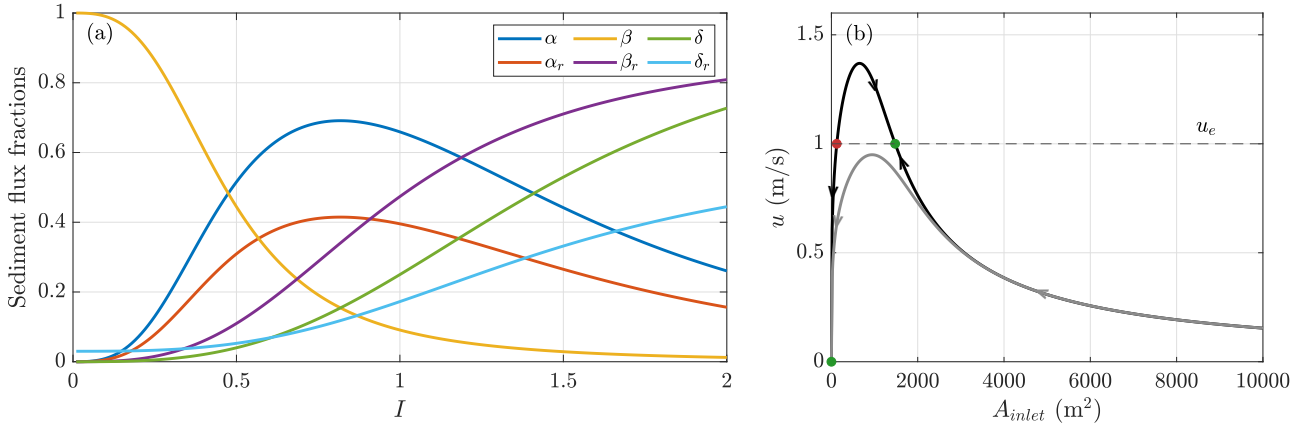

Figure S3. Implementation of inlet dynamics in the model: **(a)** Dependence of sediment transport fractions on inlet momentum balance I. Parametrizations obtained by Nienhuis and Ashton (2016). **(b)** Amplitude of the tidal current versus cross-sectional area of the inlet obtained following Escoffier's relationship. The situation depicted in grey only has one stable equilibrium (green scatter at the origin), so the inlet will tend to become narrower until closing. The situation depicted in black has two stable equilibria (green scatters), and one unstable equilibria (red scatter). In this case, the inlet will tend toward one of the two stable equilibria, depending on the region in which it is located.

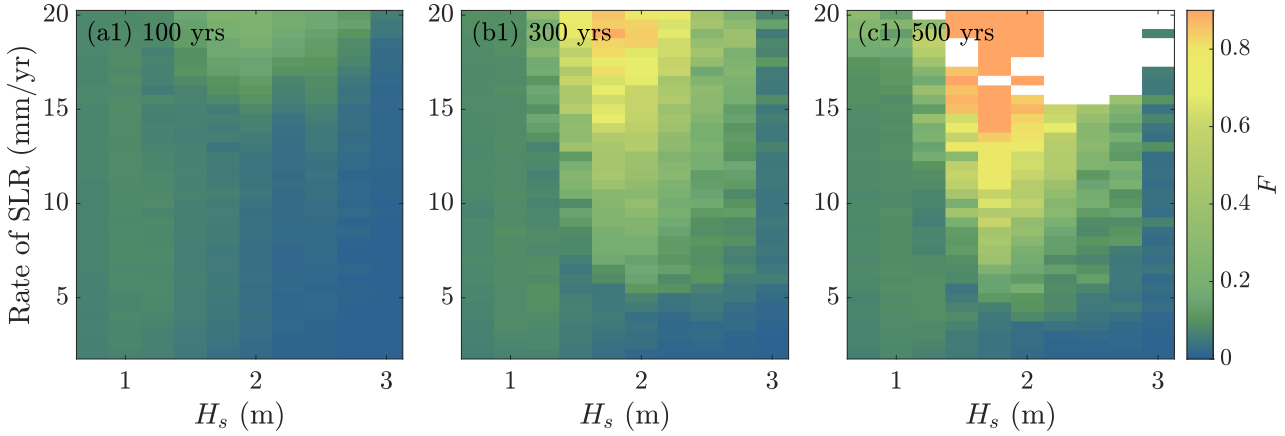

Figure S4. Alongshore fraction of the barrier lying below MSL for different values of significant wave height H_s and rate of SLR $\dot{\xi}$ at years **(a)** 2100, **(b)** 2300 and **(c)** 2500. Values shown are averages over five simulations.

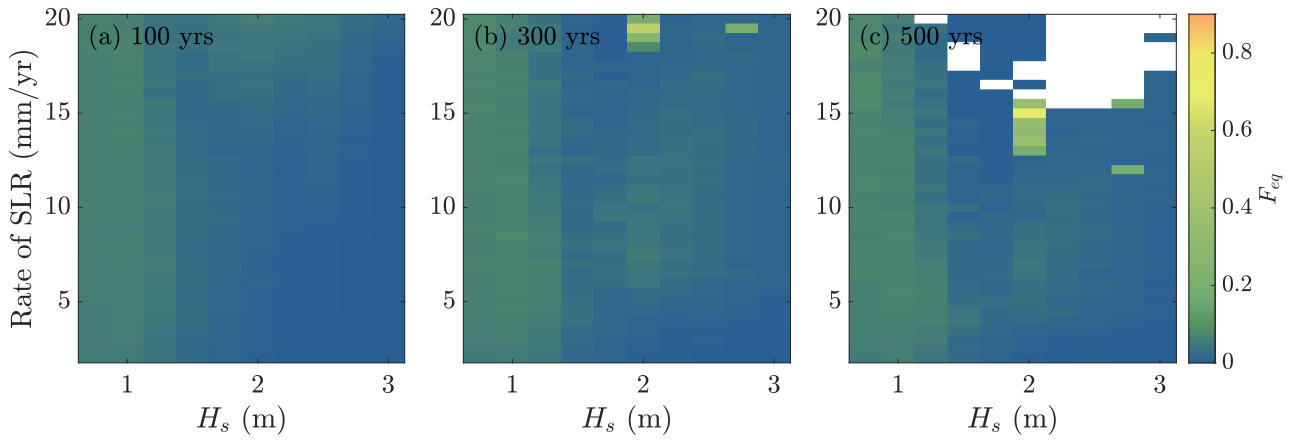

Figure S5. Alongshore fraction of the barrier lying below MSL computed assuming an equilibrium situation for different values of significant wave height H_s and rate of SLR $\dot{\xi}$ at years **(a)** 2100, **(b)** 2300 and **(c)** 2500. Values shown are averages over five simulations.

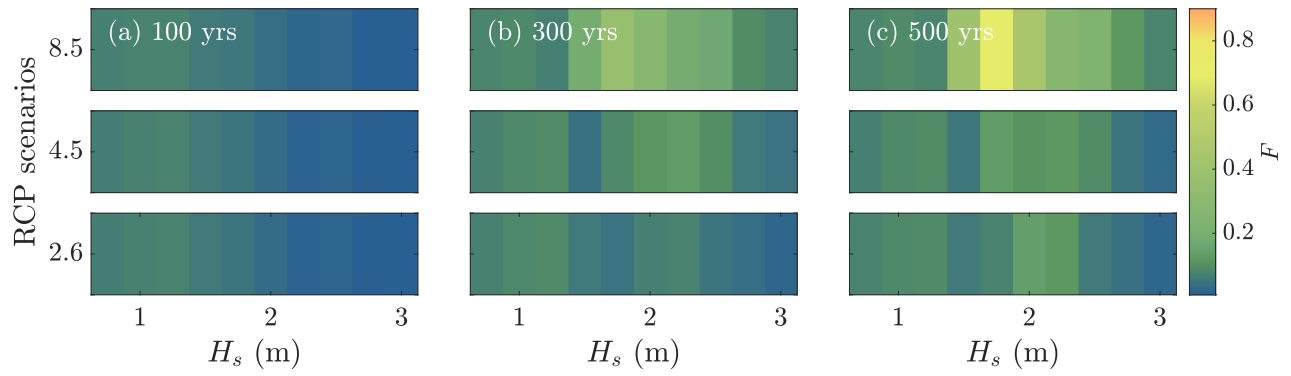

Figure S6. Alongshore fraction of the barrier lying below MSL for different values of significant wave height H_s and RCP scenarios at years **(a)** 2100, **(b)** 2300 and **(c)** 2500. Values shown are averages over five simulations.

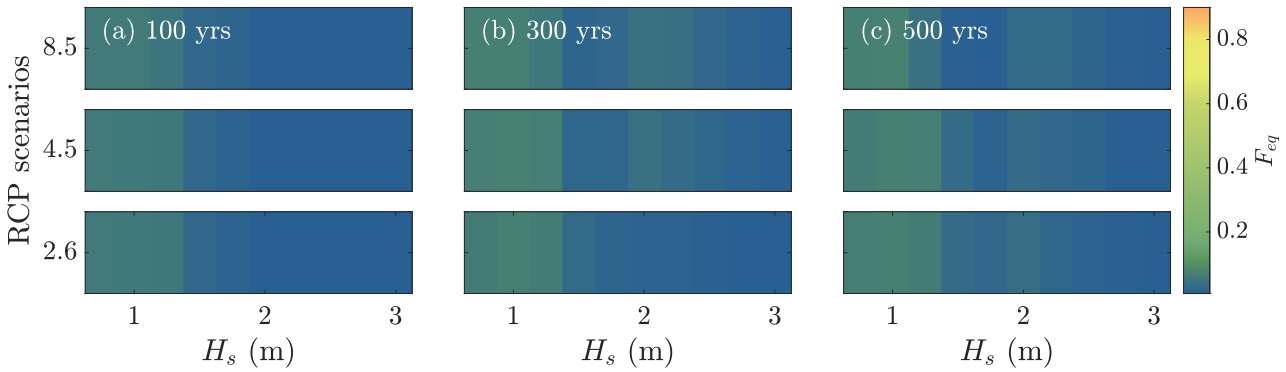

Figure S7. Alongshore fraction of the barrier lying below MSL computed assuming an equilibrium situation for different values of significant wave height H_s and RCP scenarios at years **(a)** 2100, **(b)** 2300 and **(c)** 2500. Values shown are averages over five simulations.

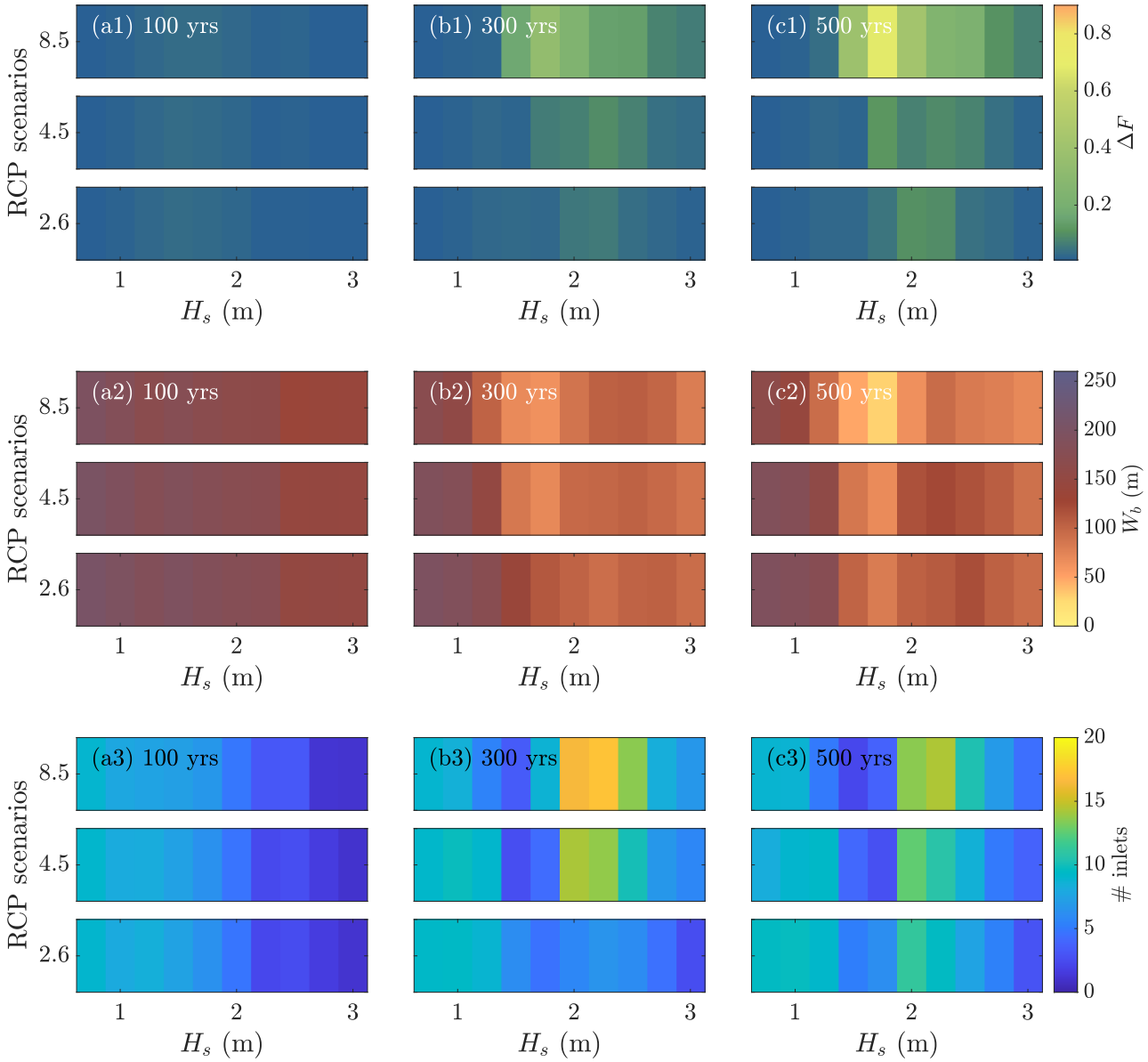

Figure S8. For different values of significant wave height H_s and RCP scenarios: color plots of ΔF **(a1,b1,c1)**, alongshore mean of barrier width W_b **(a2,b2,c2)**, and number of inlets **(a3,b3,c3)**. All three quantities are shown at years 2100, 2300, 2500 (first, second and third columns, respectively) and averaged over five simulations.